Geomechanics and Engineering, *Vol. 39, No. 1 (2024) 87-104*
https://doi.org/10.12989/gae.2024.39.1.087

Pseudo-static solution of active earth pressure against relief shelf retaining wall rotating around heel

Yun Que[a], Jisong Zhang[b], Chengcheng Long and Fuquan Chen*

College of Civil Engineering, Fuzhou University, No.2 Xueyuan Road, University Town, Fuzhou 350116, China

(*Received February 25, 2024, Revised August 25, 2024, Accepted August 26, 2024*)

Abstract. In practical engineering, the design process for most retaining walls necessitates careful consideration of seismic resistance. The prevention of retaining wall overturning is of paramount importance, especially in cases where the foundation's bearing capacity is limited. To research the seismic active earth pressure (E_S) of a relieving retaining wall rotating around base (RB), the shear dissipation graphs across various operating conditions are analyzed by using Optum software, and the earth pressure in each region was derived by the inclined strip method combined with the limit equilibrium method. By observing shear dissipation graphs across various operating conditions, the distribution law of each sliding surface is summarized, and three typical failure modes are obtained. The corresponding calculation model was established. Then the resultant force and its action point were obtained. By comparing the theoretical and numerical solutions with the previous studies, the correctness of the derived formula is proved. The variation of earth pressure distribution and resultant force under seismic acceleration are studied. The unloading plate's position, the wall heel's length, and seismic acceleration will weaken the unloading effect. On the contrary, the length of the unloading plate and the friction angle of the filling will strengthen the unloading effect. The derived formula proposed in this study demonstrates a remarkable level of accuracy under both static and seismic loading conditions. Additionally, it serves as a valuable design reference for the prevention of overturning in relieving retaining walls.

Keywords: active earth pressure; inclined slice method; RB displacement mode; relief shelf retaining wall; seismic acceleration

1. Introduction

The estimation of earth pressure has long been a crucial aspect of designing and analyzing the stability of structures like retaining walls and slopes. Taking the retaining wall as an example, various factors, such as external load, the strength of foundation soil and matric suction, also affect the magnitude and distribution of earth pressure (Lim *et al.* 2023, Fathipour *et al.* 2022). Coulomb (1776), Choudhury *et al.* (2006) and Greco (2009) considered the sliding surface as a plane and studied the earth pressure. On the other hand, Terzaghi (1943), Kerisel and Absi (1990) treated the sliding surface as a curve. Under static conditions, Some researchers (Cao *et al.* 2019, Xu *et al.* 2021, Peng 2022) derived the theoretical formula using the horizontal slice method. Cao *et al.* (2019) simplified the principal stress track line into a straight line and proposed a simplified calculation method for rigid retaining walls. Xu *et al.* (2021) proposed the analytical solution for the narrow fill of an inverted T-shaped retaining wall. Peng (2022) calculated the nonlinear distribution equation of E_a while taking shear stress into account. Chauhan and Dasaka (2016) investigated a relief shelf retaining wall (RS-RW) fracture failure in India (Fig. 1), employing finite difference numerical analysis to identify an overlooked lateral earth pressure as the primary cause.

Subsequently, Chauhan *et al.* (2021) developed a generalized closed-form mathematical expression for earth pressure distribution on RS-RWs.

Under seismic force, Nakajima *et al.* (2021) simulated the seismic resistance of a retaining wall through a series of 1-g shaking table model tests and found that the retaining wall with clay backfill was more stable than the retaining wall with sand backfill. Peng and Chen (2013) believed that the traditional Mononobe-Okabe method was not suitable for solving the earth pressure distribution problem. A more rational plastic soil wedge analysis model was established by considering the sliding surface as a plane. Iskander *et al.* (2013) extended Rankine's classical earth pressure formula based on the principle of conjugate stress and analyzed the pseudo-static force behind the rigid retaining wall of an inclined c-φ backfill soil. Different from the Mononobe–Okabe method, Fathipour *et al.* (2021) investigated the impact of anisotropic media on active and passive earth pressures acting on retaining walls. Utilizing modified pseudo-dynamic and lower limit analysis methods, they determined that seismic loads exert maximum influence under resonant conditions.

At the same time, it is possible to encounter weak foundation-bearing capacity in the actual project, resulting in foundation settlement or retaining wall overturn. From

*Corresponding author, Ph.D.
E-mail: phdchen@fzu.edu.cn
[a]Professor
E-mail: queyun_2001@fzu.edu.cn
[a]Graduate Student
E-mail: 1912801651@qq.com

ISSN: 2005-307X (Print), 2092-6219 (Online)

Fig. 1 Cantilever retaining wall with relief shelves

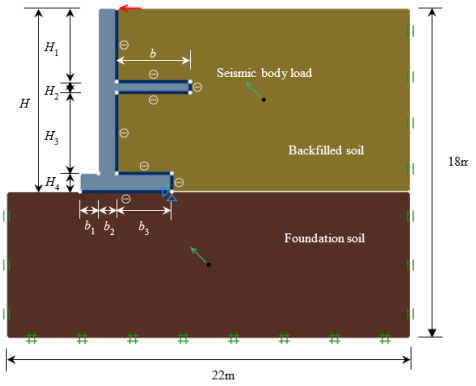

Fig. 2 Finite element limit analysis model

this, some scholars analyzed the RB motion mode of retaining walls. Thiyyakkandi *et al.* (2021) presented an *Ea* analysis approach for an inclined backfill rigid retaining wall under the RB displacement mode, assuming a logarithmic spiral sliding surface and taking the soil arch effect into account. Johari *et al.* (2016) employed gene expression programming to develop a model predicting critical design parameters of retaining walls, and assessed retaining wall reliability using finite element analysis coupled with random field theory (Johari and Maroufi 2024). Yang *et al.* (2007) and Zhang *et al.* (2022) believed that the classical earth pressure calculation method is no longer suitable for narrow backfill, RB displacement mode, and nonactive earth pressure. Therefore, Wang *et al.* (2022) improved the traditional earth pressure calculation method. The nonlinear differential layer method is used to study the influence of wall displacement and arch effect on earth pressure. Zhang *et al.* (2022) analyzed the failure mechanism of narrow fill under the RB model using the adaptive finite element analysis method. Fathipour *et al.* (2021) conducted a comprehensive study on seismic earth pressure states in retaining structures using finite element analysis and second-order cone programming (SOCP). Their research encompassed effects of material damping, anisotropy, unsaturated fill, and temperature variations (Mohamad *et al.* 2021, Bahmani *et al.* 2022). However, the influence of RS remained unexamined. Que *et al.* (2022) studied many aspects of RS-RW but did not take into account seismic load. However, in practical engineering, it is crucial to incorporate seismic design in retaining wall projects (Pain *et al.* 2015, Srikar *et al.* 2021).

Thus, OptumG2 is used to simulate the RB displacement mode of the RS-RW under seismic load and study its failure mode under the active limit state. The study results revealed the distribution pattern of the sliding surface and established a corresponding calculation model for E_s. The calculation formula of E_s is derived by the inclined slice method combined with the limit equilibrium method. The seismic acceleration's impact is analyzed by comparing the results of the formula and numerical method.

2. Study on failure mode

2.1 Finte element model

OptumG2 is a finite element and limit analysis software (FELA) tailored for geotechnical engineering applications. By employing advanced numerical algorithms, it efficiently computes both lower and upper bounds, offering timely estimates of the exact solution and associated error margins. Unlike traditional limit equilibrium methods, FELA autonomously refines the plastic region and visualizes results, facilitating rapid convergence toward the optimal solution while enhancing computational efficiency.

In Fig. 2, OptumG2 is used to study the failure mode of the RS-RW with infinite-width filled soil rotating around the wall heel to reach the active limit state under seismic load. The wall is considered as a rigid body and the linear elastic model is adopted. The wall–soil interface friction angle is replaced by a reduction coefficient. Homogeneous and isotropic sand behind the wall, using the Mohr-Coulomb constitutive model. Without considering the foundation soil settlement and deformation, the retaining wall's bottom is considered to be completely smooth. And the foundation soil is considered to be a hard plastic clay in a stable state, while Table 1 provides a summarized overview of the parameters for the retaining wall, backfill, and foundation soil.

The retaining wall is 10 m high, the wall back is upright, the wall is 1 m thick, and the unloading plate is 0.6 m thick.

Eq. (1) shows the related variable definitions.

$$\begin{cases} m = H_1 / H & 2\text{m} \le H_1 \le 5\text{m} \\ l = b / H & 1\text{m} \le b \le 4\text{m} \\ n = b_3 / H & b_3 = 3\text{m} \end{cases} \tag{1}$$

In Optum G2, seismic forces generated by an earthquake are represented as seismic body load within the soil, using horizontal (k_h) and vertical (k_v) acceleration coefficients. These body loads are similarly applied to both gravity retaining walls and foundation soils. Given the significant uncertainty in both the magnitude and direction of seismic acceleration, the most adverse conditions are typically considered.

To eliminate the boundary effect, the model size was verified to be 22 m × 18 m. The bottom displacement boundary condition for the model is configured as the standard boundary condition., the left and right normal boundary conditions, and the model's top boundary was free. To ensure that the wall reaches its limit state under the RB displacement mode, a concentrated horizontal multiplier load is applied at the top of the wall. This load restricts both

Table 1 Parameters of wall, backfilled and foundation soil

/	Material	Cohesive c(kPa)	Internal friction φ(°)	Gravity γ(kN/m^3)	Young's modulus E (MPa)	Poisson's ratio v
Retaining wall	Rigid body	/	/	25	/	/
Backfilled soil	Dense sand	0	30	18	40	0.3
Foundation soil	Hard plastic clay	20	22	21	50	0.25

horizontal and vertical displacement, allowing only rotation around the wall heel. The mesh is configured using the lower-bound six-node triangular isoparametric elements, with an initial mesh count of 10,000. Initial stresses are established using the K_0 process.

2.2 The description of FELA

Limit equilibrium is grounded in the principles of static equilibrium. This method typically requires an initial assumption of the failure surface shape and analysis using moment and force equilibrium equations (Cao *et al.* 2019), and the accuracy of results is constrained by the assumption of the failure surface. Traditional limit analysis, an analytical approach, employs the universal theorems of an ideal elastic-plastic body in its limit state—the upper bound and lower bound theorems—to determine the ultimate load. However, this method demands substantial computational resources, particularly for complex structures, and often necessitates the use of numerical methods. The OptumG2 software utilized in this study integrates limit analysis with finite element analysis. It performs three adaptive iterations based on shear dissipation energy, automates mesh refinement in plastic regions, and provides visualization of results, allowing rapid convergence to the optimal solution and enhancing computational efficiency. This approach is particularly suitable for investigating the plastic region of the backfill behind the retaining wall following failure under RB displacement mode.

2.3 Influence of various parameters on the failure mode

A large number of models were observed to study the failure mode of the wall. The shear dissipation cloud image under the limit state was intercepted, as shown below. The total displacement $|\mu|$ at the top of the wall, and the slip plane and the horizontal plane angle α are related to the following factors. Control single variable, an imaginary wall back is used for calculation in this paper, the friction coefficient of the wall-soil interface is assigned to a constant value of 0.33.

2.3.1 Relief shelf position

Fig. 3 illustrates the distribution pattern of the sliding surface behind the wall as the unloading plate
position changes, obtained through soil shear dissipation. The parameters considered in this study include seismic acceleration, the relative length of the unloading plate, the relative length of the wall heel, and the internal friction angle of fill are kept unchanged, which are k_h = 0.1, k_v =

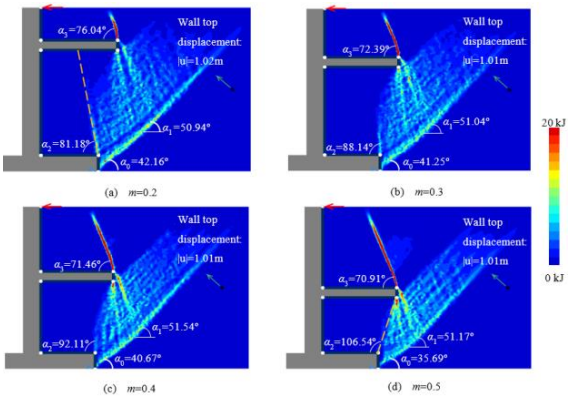

Fig. 3 Shear dissipation diagram of soil under different relief shelf positions

0.1, l = 0.4, n = 0.3, and φ = 30°, respectively. The distribution of failure sliding surfaces under four working conditions is studied, and it is found that the three sliding surfaces are affected by the RS's position.

The initial sliding surface behind the wall is a composite curve comprising both a curved portion and a straight line. As the RS's position increases, the curved portion's curvature decreases, causing the intersection point between the curve and the straight line to shift downwards. It is regarded as a broken line to simplify the calculation. With the increase of the RS's position, the dip angle of the first section of the broken line decreased from 42.16° to 35.69°, while the dip angle of the second section remained unchanged. The position of the unloading plate has a significant impact on the second sliding surface. As the distance between the plate and the top of the wall increases from 2 m to 5 m, the sliding surface's distribution changes from contact with the bottom of the unloading plate (Fig. 3(a)) to contact with the end of the unloading plate (Fig. 3(d)), while the dip angle increases from 81.18° to 106.54°. Concerning the third sliding surface, it varies according to the position of the unloading plate, causing the dip angle to decrease from 76.04° to 70.91°. The sliding surface is approximately a curve when m=0.2, while it is approximately straight when m ≥ 0.3. In general, with the deepening of the location of the unloading plate, the overlying soil weight on the unloading plate increases, and the overlying soil weight on the wall heel decreases, which may reduce the retaining wall stability to some extent.

2.3.2 Relief shelf length

Fig. 4 shows the distribution law of failure sliding surface of fill behind the wall under the change of RS's length, where m = 0.4 and other parameters don't change. With the wall reaches the limited state of activity, the soil is

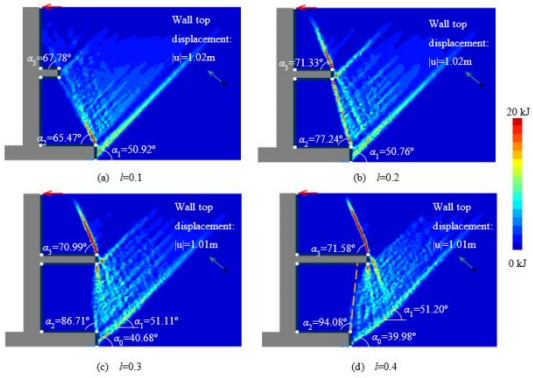

Fig. 4 Shear dissipation diagram of soil under different relief shelf lengths

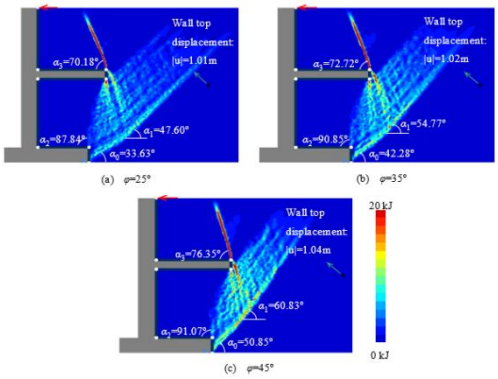

Fig. 5 Shear dissipation diagram of soil under different internal friction angles of backfill

constantly damaged along the depth, and the small sliding surface is generated. The figure shows that there are many cross-distribution phenomena of sliding surfaces in the damaged wedge. Some scholars (Que *et al.* 2022 and Zhang *et al.* 2022) refer to these sliding surfaces as sub-sliding surfaces. As the RS's length increases, the first sliding surface's distribution transitions from a straight line to a broken line. Simultaneously, the dip angle of the second sliding surface exhibits a significant increase, growing from 65.47° to 94.08°. and the distribution state changed from being connected to the relief shelf end to being connected to the relief shelf bottom, thus exerting the unloading effect. The dip angle of the third sliding surface increased from 67.78° to 71.58°. As shown in Fig. 4(a), if $0<l<0.1$, the third sliding surface will disappear, and the second sliding surface will over the relief shelf, directly be connected with the retaining wall vertical arm. The distribution law is consistent with that of the cantilever retaining wall. In summary, the dip angle of the second and third sliding surfaces increase leads to the entire sliding wedge decrease and the E_s decrease.

2.3.3 Internal friction angle of the backfill soil

Fig. 5 shows the distribution law of the failure sliding surface of the backfill under the friction angle (φ) change, which are 25°, 35°, and 45°. The limit analysis findings reveal that when the friction angle increases, so does the dip angle of three sliding surfaces, as well as the displacement

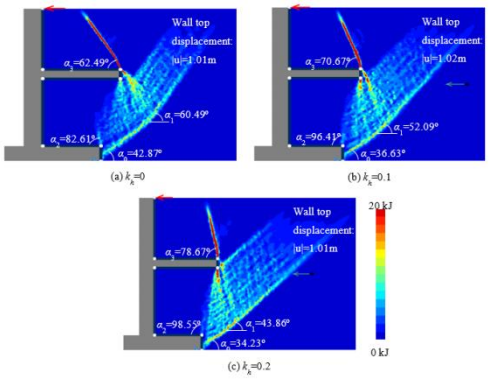

Fig. 6 Shear dissipation diagram of soil under different horizontal seismic accelerations

of the top wall. The two dips of the first sliding surface increased from 33.63° and 47.60° to 50.85° and 60.83°, respectively. The dip angle of the second sliding surface increased from 87.87° to 91.07°. The dip angle of the third sliding surface increased from 70.18° to 76.35°. When the geometric conditions of the retaining wall remain unchanged, the increase of the dip angles of each sliding surface will lead to the decrease of the area of the failure wedge. The failure pattern observed in this study is consistent with the theoretical concept that the internal friction angle of the fill material increases, increasing the interlocking resistance and shear strength of the soil, and a decrease in the soil pressure, proving the reliability of the shear dissipation diagram.

2.3.4 Horizontal seismic acceleration coefficient

Fig. 6 shows the distribution law of the sliding surface of fill under varying horizontal seismic acceleration coefficient (k_h) values of 0, 0.1, and 0.2. The vertical acceleration coefficient remains constant at k_v = 0. The figure shows that horizontal acceleration has no effect on the wall top's displacement. The comparison between Figs. 6(a) and 6(c) shows that the difference between the two dips of the first sliding surface becomes smaller and gradually becomes a straight line (α_0 = 34.23°, α_1 = 43.86°) from a broken line (α_0 = 42.87°, α_1 = 60.49°). With the increase of horizontal acceleration, the dip angles of the second and third sliding surfaces increased from 82.61° and 62.49° to 98.55° and 78.67°, respectively. Additionally, as depicted in Fig. 6(a), the second sliding surface reaches to the RS's bottom. As the horizontal acceleration increases, the second sliding surface extends closer to the RS's end, and the unloading effect gradually weakens, indicating that the horizontal acceleration of the seismic will weaken the unloading effect

2.3.5 Vertical seismic acceleration coefficient

Fig. 7 illustrates the distribution pattern of the failure sliding surface behind the wall as the vertical seismic acceleration undergoes variations. The horizontal seismic acceleration coefficient k_h = 0.1, and the vertical seismic acceleration coefficient is k_v = 0, 0.1, and 0.2. The comparison of k_v = 0 and k_v = 0.2 showed the following results: α_0 increased from 36.63° to 39.21° with increasing

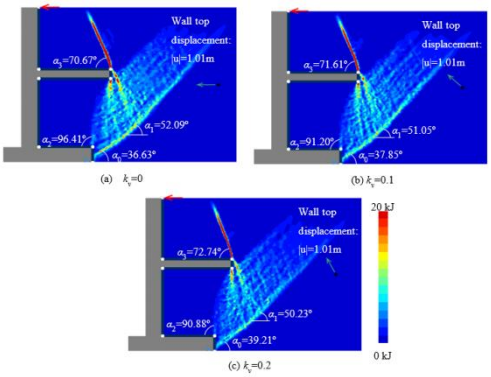

Fig. 7 Shear dissipation diagram of soil under different vertical seismic accelerations

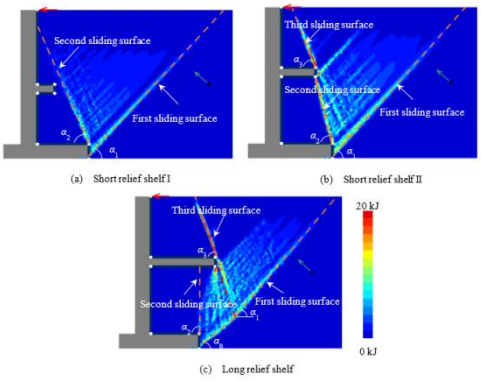

Fig. 8 Three typical failure modes

vertical acceleration, α_1 decreased from 52.09° to 50.23° with increasing vertical acceleration, α_2 decreased from 96.41° to 90.88° with increasing vertical acceleration, and α_3 increased from 70.67° to 72.74° with increasing vertical acceleration. With the decrease of α_2, the contact point between the second sliding surface and the relief shelf bottom gradually moves to the left, indicating that the vertical seismic acceleration enhances the unloading effect. The comparison between shear dissipation maps of soil mass under seismic acceleration showed that horizontal seismic acceleration more significantly affects the dip angles of sliding surfaces.

2.4 Three typical failure modes

The shear dissipation diagram corresponding to a large number of working conditions was studied according to the analysis of failure modes under different parameters. In Fig. 8, the sliding surface's distribution state was summarized, highlighting three distinct failure modes. Fig. 8(a) demonstrates the first mode, known as short relief shelf I, where the first sliding surface aligns as a straight line from the wall heel to the fill surface. The second sliding surface, passing through the relief shelf, is also a straight line from the wall heel to the vertical arm. The initial sliding surface's distribution law stays unaltered, as illustrated in Fig. 8(b). The second sliding surface interfaces with the upper and lower ends of the unloading plate to generate a third sliding plane, which subsequently contacts the surface of the backfill. This failure mode is short relief shelf II. In Fig. 8(c), the unloading plate further becomes longer. The first sliding surface is the broken line between the wall heel and the fill surface. The second sliding distribution law remains unchanged, but the intersection point with the unloading plate moves to the left. Moreover, the third sliding distribution law remains unchanged, and this failure mode is the long relief shelf.

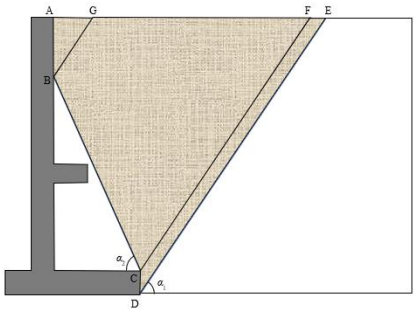

Fig. 9 Pseudo-static calculation model of short relief shelf I

3. Calculation method of earth pressure

The results of limit analysis show that when the retaining wall in RB displacement mode reaches the active limit state, there will be many parallel sliding surfaces in the plastic region, constituting the whole sliding wedge. The inclined strip method can be used to solve the pseudo-static solution of the Es, combined with the sliding surfaces's distribution in the sliding wedge. The basic assumptions of the calculation method are as follows:

(1) The RW's rotation around its heel brings the soil behind it in close proximity to the active limit condition.

(2) The RW is a hard body, and the semi-infinite width backfill behind the wall is homogeneous sand, isotropic and obeys the Mohr-Coulomb criterion.

(3) The seismic load is simulated by horizontal and vertical acceleration.

(4) The RS-RW can be approximated as a double-layer cantilever retaining wall. It is assumed that the sliding surface extending from the RS's bottom makes an angle of α_1 with the horizontal plane

3.1 Short relief shelf I

Fig. 9 illustrates the calculated model for Short I based on the summary of the FELA. Because the relief shelf's length is short, there is no unloading effect, and the sliding surface's distribution is consistent with the cantilever retaining wall. The plastic failure zone behind the wall can be partitioned into three distinct sections for meticulous analysis, wherein the soil pressure shall be calculated correspondingly.

3.1.1 Calculation in the ABG area

Fig. 10 shows the distribution of the forces on the soil wedge ABG. The left side is subjected to the force E_{w0} of

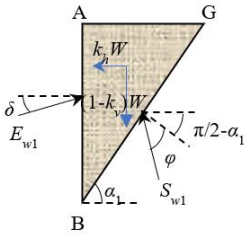

Fig. 10 Force analysis of ABG region

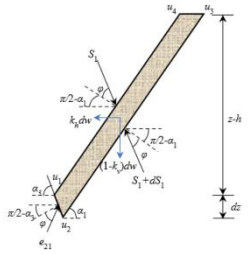

Fig. 11 Stress analysis of soil strip $u_1u_2u_3u_4$

the RW arm on the sliding wedge, and the angle with the horizontal direction is δ. The right side is subjected to the force S_{w0} applied by the BCFG region, and the angle with the horizontal direction is $\pi/2-\alpha_1+\varphi$. The surface of the wedge is horizontal, and there is no external load. Under the effect of seismic force, the gravity of the wedge itself is transformed into horizontal inertial force k_hW_0 and vertical inertial force $(1-k_v)W_0$. The unloading effect does not affect the failure mode of relief shelf I; thus, the earth pressure is approximately linearly distributed, which can be solved by the block method. Moreover, the active earth pressure E_{w0} of the RW in the ABG area is obtained.

Horizontal direction

$$E_{w0}\cos\delta = k_hW_0 + S_{w0}\cos\left(\pi/2-\alpha_1+\varphi\right) \tag{2}$$

Vertical direction

$$E_{w0}\sin\delta + S_{w0}\sin\left(\pi/2-\alpha_1+\varphi\right) = \left(1-k_v\right)W_0 \tag{3}$$

Where

$$\begin{cases} W_0 = \dfrac{\gamma {h_{w0}}^2 \cot\alpha_1}{2} \\ h_{w0} = \left(0.9 - n\cot\alpha_2\right)H \end{cases} \tag{4}$$

Combining Eqs. (2)-(4), the resultant force on the ABG area is as follows

$$E_{w0} = C_{w0}\gamma {h_{w0}}^2 \cot\alpha_1 \tag{5}$$

$$\begin{cases} C_{w0} = \dfrac{\left[k_h\sin\theta_1 + \left(1-k_v\right)\cos\theta_1\right]}{2\sin\left(\theta_1+\delta\right)} \\ \theta_1 = \dfrac{\pi}{2} - \alpha_1 + \varphi \end{cases} \tag{6}$$

Since the AB side is located in the RW arm, the earth pressure acting on this area is linearly distributed along the wall height, so the normal earth pressure coefficient at the AB of the retaining wall arm is

$$K_{w0} = \frac{2E_{w0}}{\gamma {h_{w0}}^2} \tag{7}$$

The normal earth pressure expression is as follows

$$\sigma_{nw0} = K_{w0}\gamma z \quad 0 \le z < h_{w0} \tag{8}$$

3.1.2 Calculation in the BCFG area

As depicted in Fig. 11, the earth pressure will mutate at point B, given that the BC edge represents the hypothetical wall back and the AB edge represents the actual wall back. Thus, the inclined slice method is used to analyze the force of the BCFG area. The u_1u_2 side is subjected to the force e_{21} of the hypothetical wall back to the soil strip, and the angle with the horizontal direction is $\pi/2-\alpha_2+\varphi$. The u_1u_4 edge and u_2u_3 edge are subjected to the interaction force between the soil strips, which are S_1 and S_1+dS_1, respectively, and the angle with the horizontal direction is $\pi/2-\alpha_1+\varphi$. The soil strip is subjected to inertial forces k_hdw and $(1-k_v)dw$ from seismic acceleration.

Horizontal direction

$$e_{21}\frac{dz}{\sin\alpha_2}\cos\theta_2 = k_hdw + dS_{21}\cos\theta_1 \tag{9}$$

Vertical direction

$$e_{21}\frac{dz}{\sin\alpha_2}\sin\theta_2 + dS_{21}\sin\theta_1 = \left(1-k_v\right)dw \tag{10}$$

Where

$$dw = \frac{1}{2}\left(\frac{z}{\sin\alpha_1} + \frac{z+dz}{\sin\alpha_1}\right)\gamma\frac{dz}{\sin\alpha_2}\sin\left(\alpha_1+\alpha_2\right) \tag{11}$$

Ignoring the second-order differential variables,

$$dw = \gamma z dz\left(\cot\alpha_1 + \cot\alpha_2\right) \tag{12}$$

Combining Eqs. (9) and (10) and Eq. (12), the earth pressure's distribution function in the BCFG region is obtained as follows

$$e_{21} = C_{21}\gamma z\sin\alpha_2 \quad h_{w1} < z < 0.9H \tag{13}$$

Where

$$\begin{cases} C_{21} = \dfrac{\left(\cot\alpha_1+\cot\alpha_2\right)}{\sin\left(\theta_1+\theta_2\right)}\left[k_h\sin\theta_1 + \left(1-k_v\right)\cos\theta_1\right] \\ \theta_2 = \pi/2 - \alpha_2 + \varphi \end{cases} \tag{14}$$

Integrating Eq. (13), the resultant force acting on the imaginary wall back is as follows

$$E_{21} = \int_{h_{w1}}^{0.9H} e_{21}dz \tag{15}$$

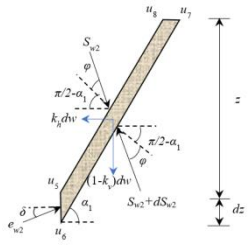

Fig. 12 Stress analysis of soil strip $u_5u_6u_7u_8$

The resultant action point's position is as follows

$$Z_{21}=\frac{\int_{h_{w1}}^{0.9H}e_{21}(H-z)dz}{E_{21}} \tag{16}$$

3.1.3 Calculation in the CDEF area

As shown in Fig. 12, the CDEF area is at the heel end of the wall. The stress analysis of any soil strip is conducted. The u_5u_6 side is completely vertical, and ew_2 is exerted by the wall heel on the sliding wedge, showing a δ angle with the horizontal direction. u_5u_8 and u_6u_7 are subjected to wedge interactions S_{w2} and $S_{w2}+dS_{w2}$, respectively, and the horizontal angles of both are $\pi/2-\alpha_1+\varphi$. The soil strip itself is subjected to the inertial force equivalent to the seismic acceleration.

Horizontal direction

$$e_{w2}dz\cos\delta=k_h dw+dS_{w2}\cos\theta_1 \tag{17}$$

Vertical direction

$$e_{w2}dz\sin\delta+dS_{w2}\sin\theta_1=(1-k_v)dw \tag{18}$$

Where

$$dw=\frac{1}{2}\left(\frac{z}{\sin\alpha_1}+\frac{z+dz}{\sin\alpha_1}\right)\gamma dz\cos\alpha_1 \tag{19}$$

Ignoring the second-order differential variables

$$dw=\gamma z dz\cot\alpha_1 \tag{20}$$

Combining Eqs. (17)-(18) and Eq. (20), the distribution function of the earth pressure acting on the heel is obtained as follows

$$e_{w2}=C_{w2}\gamma z\cot\alpha_1 \tag{21}$$

Where

$$C_{w2}=\frac{k_h\sin\theta_1+(1-k_v)\cos\theta_1}{\sin(\delta+\theta_1)} \tag{22}$$

By integrating Eq. (21) along the depth, the resultant earth pressure at the heel can be obtained as follows

$$E_{w2}=\int_{0.9H}^{H}e_{w2}dz \tag{23}$$

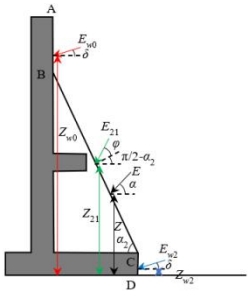

Fig. 13 Application points of earth pressure and resultant force in each region of short relief shelf I

The position of the resultant force action point is as follows:

$$Z_{w2}=\frac{\int_{0.9H}^{H}e_{w2}(H-z)dz}{E_{w2}} \tag{24}$$

3.1.4 The total resultant force of Es and its point of application

As shown in Fig. 13, it acts on the earth pressure resultant force position of the retaining wall. Due to the linear distribution of normal forces in the ABG region, E_{w0} acts on one-third of the height of AB. The positions of E_{21} and E_{w2} are obtained from Eqs. (16) and (24).

The resultant earth pressure in each region is decomposed into horizontal and vertical directions as follows

$$\begin{cases}E_{w0}\cos\delta+E_{21}\cos\theta_2+E_{w2}\cos\delta=E\cos\alpha\\E_{w0}\sin\delta+E_{21}\sin\theta_2+E_{w2}\sin\delta=E\sin\alpha\end{cases} \tag{25}$$

The resultant force of seismic earth pressure is as follows

$$\begin{cases}E_s=\dfrac{E_{w0}\cos\delta+E_{21}\cos\theta_2+E_{w2}\cos\delta}{\cos\alpha}\\\alpha=\arctan\dfrac{E_{w0}\sin\delta+E_{21}\sin\theta_2+E_{w2}\sin\delta}{E_{w0}\cos\delta+E_{21}\cos\theta_2+E_{w2}\cos\delta}\end{cases} \tag{26}$$

The resultant force action point is calculated by balancing the bending moment

$$\begin{cases}Z=\dfrac{0.1H\cot\alpha_2}{\cot\alpha+\cot\alpha_2}+\dfrac{M_{w0}+M_{21}+M_{w2}}{E(\cos\alpha+\cot\alpha_2\sin\alpha)}\\M_{w0}=E_{w0}(Z_{w0}\cos\delta+nH\sin\delta)\\M_{21}=E_{21}\left[Z_{21}\cos\theta_2+(Z_{21}-0.1H)\cot\alpha_2\sin\theta_2\right]\\M_{w2}=E_{w2}Z_{w2}\cos\delta\end{cases} \tag{27}$$

3.2 Short relief shelf II

Fig. 14 shows the model for short relief shelf II, which can be divided into four areas, namely, upper retaining wall area (ABI), relief shelf area (BCHI), lower retaining wall area (CDGH), and wall heel area (DEFG). The ABI region is located at the upper part of the RS, which is not affected

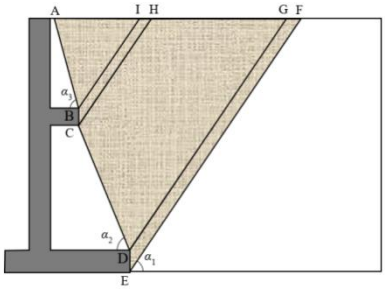

Fig. 14 Pseudo static calculation model of short relief shelf II

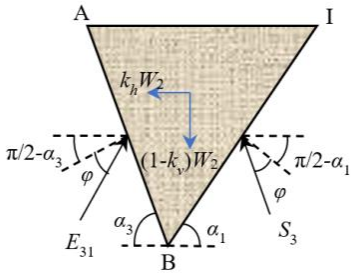

Fig. 15 Force analysis of ABL region

by the RS, and is directly solved by the block method. In the other three regions, there is an interaction force between wedges on both sides; thus, using the inclined strip method is more convenient to solve it.

3.2.1 Calculation in the ABI area

In Fig. 15, the stress analysis of block ABI is presented, wherein the AB edge experiences the force E_{31} exerted by the imaginary wall onto the block. The angle between the AB edge and the horizontal direction is given by $\pi/2-\alpha_3+\varphi$. The weight of the block is W_2, which is affected by seismic acceleration.

Horizontal direction

$$E_{31}\cos\theta_3 = k_h W_2 + S_3\cos\theta_3 \tag{28}$$

Vertical direction

$$E_{31}\sin\theta_3 + S_3\sin\theta_1 = (1-k_v)W_2 \tag{29}$$

Where

$$\begin{cases} W_2 = \dfrac{\gamma h_{31}^{\ 2}}{2}\left(\cot\alpha_1 + \cot\alpha_3\right) \\ h_{31} = mH \end{cases} \tag{30}$$

Combining Eqs. (28)-(29) and Eq. (30), the earth pressure acting on the ABI region is obtained as follows

$$E_{31} = C_{31}\frac{\gamma h_{31}^{\ 2}}{2}\left(\cot\alpha_1 + \cot\alpha_3\right) \tag{31}$$

$$\begin{cases} C_{31} = \dfrac{k_h\sin\theta_1 + (1-k_v)\cos\theta_1}{\sin(\theta_1+\theta_3)} \\ \theta_3 = \pi/2 - \alpha_3 + \varphi \end{cases} \tag{32}$$

The regional ABI is situated on the upper section of the RS and remains unaffected by the unloading effect, resulting in a linear distribution of E_s. Consequently, the coefficient for the imaginary wall back is as follows

$$K_{31} = \frac{2E_{31}}{\gamma h_{31}^{\ 2}} \tag{33}$$

The normal earth pressure expression is as follows

$$\sigma_{n31} = K_{31}\gamma z \quad 0 \le z < h_{31} \tag{34}$$

3.2.2 Calculation in the BCHI and DEFG areas

In Fig. 14, the calculating procedure of the earth pressure in the BCHI and DEFG areas is the same as the CDEF area in short relief shelf I. The resultant force of the two regional walls on the sliding wedge is as follows

$$E_{w1} = \int_{mH}^{(m+0.06)H} e_{w1}dz \tag{35}$$

$$E_{w2} = \int_{0.9H}^{H} e_{w2}dz \tag{36}$$

The action points of the resultant force in the two areas are as follows

$$Z_{w1} = \frac{\int_{mH}^{(m+0.06)H} e_{w1}(H-z)dz}{E_{w1}} \tag{37}$$

$$Z_{w2} = \frac{\int_{0.9H}^{H} e_{w2}(H-z)dz}{E_{w2}} \tag{38}$$

3.2.3 Calculation in the CDGH area

In Fig. 14, the method of analyzing soil pressure in the CDGH region can be referenced from Section 3.1.2, which is consistent with the analysis conducted for the BCFG region. The computational results are presented as follows

$$E_{21} = \int_{(m+0.06)H}^{0.9H} e_{21}dz \tag{39}$$

$$Z_{21} = \frac{\int_{(m+0.06)H}^{0.9H} e_{21}(H-z)dz}{E_{21}} \tag{40}$$

3.2.4 The total resultant force of Es and its point of application

Fig. 16 illustrates the directions and locations of the combined earth pressure forces in the divided areas mentioned above. In particular, the force E_{31} acts at one-third of the height of the wall face AB.

The seismic earth pressure resultant force E is solved by decomposing the earth pressure in each region into horizontal and vertical directions:

$$\begin{cases} E_{31}\cos\theta_3 + E_{w1}\cos\delta + E_{21}\cos\theta_2 + E_{w2}\cos\delta = E\cos\alpha \\ E_{31}\sin\theta_3 + E_{w1}\sin\delta + E_{21}\sin\theta_2 + E_{w2}\sin\delta = E\sin\alpha \end{cases} \tag{41}$$

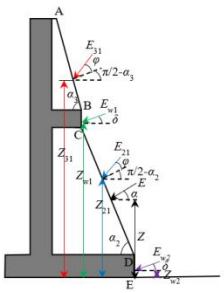

Fig. 16 Application points of earth pressure and resultant force in each region of short relief shelf II

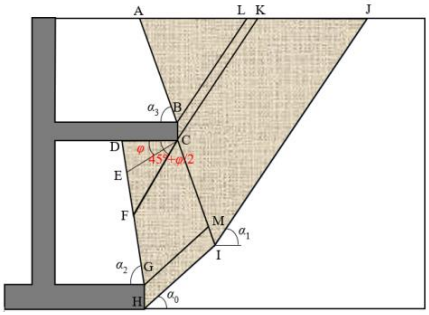

Fig. 17 Pseudo static calculation model of long relief shelf

E_s and its action angle α are obtained as follows

$$\begin{cases} E_s = \dfrac{E_{31}\cos\theta_3 + E_{w1}\cos\delta + E_{21}\cos\theta_2 + E_{w2}\cos\delta}{\cos\alpha} \\ \alpha = \arctan\dfrac{E_{31}\sin\theta_3 + E_{w1}\sin\delta + E_{21}\sin\theta_2 + E_{w2}\sin\delta}{E_{31}\cos\theta_3 + E_{w1}\cos\delta + E_{21}\cos\theta_2 + E_{w2}\cos\delta} \end{cases} \tag{42}$$

The position of the action point of E can be obtained by balancing the bending moment around the wall heel

$$\begin{cases} Z = \dfrac{0.1H\cot\alpha_2}{\cot\alpha + \cot\alpha_2} + \dfrac{M_{31} + M_{w1} + M_{21} + M_{w2}}{E\left(\cos\alpha + \cot\alpha_2\sin\alpha\right)} \\ M_{31} = E_{31}Z_{31}\cos\theta_3 + E_{31}\left[0.5\left(H - Z_{31}\right)\cot\alpha_3 + \left(n-l\right)H\right] \\ M_{w1} = E_{w1}\left[Z_{w1}\cos\delta + \left(n-l\right)H\sin\delta\right] \\ M_{21} = E_{21}\left[Z_{21}\cos\theta_2 + \left(Z_{21} - 0.1H\right)\cot\alpha_2\sin\theta_2\right] \\ M_{w2} = E_{w2}Z_{w2}\cos\delta \end{cases} \tag{43}$$

3.3 Long relief shelf

The computational model for the long unloading plate mode is depicted in Fig. 17. The diagram shows that the failure soil wedge can be divided into five areas, namely, the upper retaining wall area (ABL), the relief shelf area (BCKL), the unloading effect area (DFC), the area not affected by the unloading effect (FGMC), and the wall heel area (GHIM). The quasi-static solution of the E_s is calculated.

As indicated in Fig. 17, the angle between the left side of the ABL region and the horizontal direction is denoted as α_3, while the right angle is denoted as α_1. The left side of the BCKL region is vertical, and α_1 is the right angle. α_2 is the angle formed by the CIJK region's left side and the horizontal direction, and α_1 represents the right. The stress of these three areas is consistent with the stress of areas ABI, BCHI, and CDGH in short relief shelf II, and the earth pressure is calculated directly by Eq. (31) and Eq. (35) and Eq. (39).

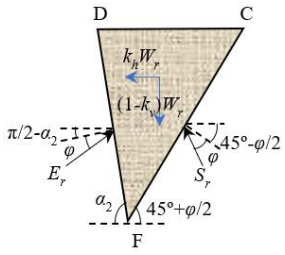

Fig. 18 Force analysis of DFC region

3.3.1 Calculation in the DFC area

According to the research of Klein (1964), the edge DC's earth pressure beneath the unloading plate can be considered zero, and the force in the DFC region is similar to that in the ABL region, as shown in Fig. 18.

The DF side is subjected to the force E_r exerted by the imaginary wall back on the soil, and the angle from the horizontal direction is $\pi/2\text{-}\alpha_2+\varphi$. According to the assumption of Klein (1964), the angle of the FC edge is $45°+\varphi/2$, which is subjected to the interaction force S_r between soils. The angle between S_r and the horizontal direction is $45°+\varphi/2$. The self-weight of block in DFC is W_r, which can be decomposed into the inertial force in horizontal and vertical directions under the action of earthquake acceleration.

Horizontal direction

$$E_r\cos\theta_2 = k_hW_r + S_r\cos\left(45° + \varphi/2\right) \tag{44}$$

$$E_r\sin\theta_2 + S_r\sin\left(45° + \varphi/2\right) = \left(1 - k_v\right)W_r \tag{45}$$

Where

$$\begin{cases} W_r = \dfrac{\gamma h_r^2}{2}\left[\cot\alpha_2 + \cot\left(45° + \varphi/2\right)\right] \\ h_r = \dfrac{l - n + \left(0.84 - m\right)\cot\alpha_2}{\cot\alpha_2 + \cot\left(45° + \varphi/2\right)}H \end{cases} \tag{46}$$

Combining Eqs.(44)-(45) and Eq. (47), the earth pressure acting on the DFC region is obtained as follows

$$E_r = \frac{1}{2}C_r\gamma h_r^2 \tag{47}$$

$$C_r = \frac{k_h\sin\left(45° + \varphi/2\right) + \left(1 - k_v\right)\cos\left(45° + \varphi/2\right)}{\sin\left[\theta_2 + \left(45° + \varphi/2\right)\right]}\left[\cot\alpha_2 + \cot\left(45° + \varphi/2\right)\right] \tag{48}$$

Therefore, the normal earth pressure coefficient of the imaginary wall back is as follows

$$K_r = \frac{2E_r\cos\varphi}{\gamma h_r^2} \tag{49}$$

The normal earth pressure expression is as follows

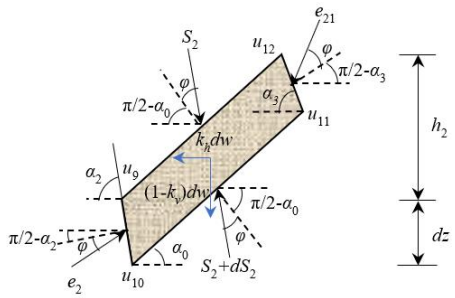

Fig. 19 Force analysis of soil strip $u_9u_{10}u_{11}u_{12}$

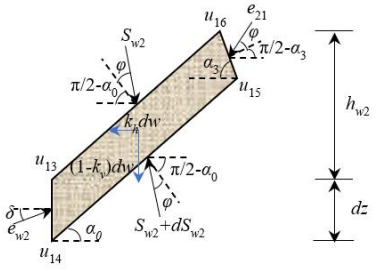

Fig. 20 Stress analysis of soil strip $u_{13}u_{14}u_{15}u_{16}$

$$\sigma_{nr}=K_r\gamma\left[z-(m+0.06)H\right]\quad (m+0.06)H\le z<(m+0.06)H+h_r \tag{50}$$

3.3.2 Calculation in the FGMC area

Since the four edges of the FGMC area are affected by forces, the calculation is complicated, and the earth pressure on the edge of FG only needs to be calculated in this paper, so it is more convenient to use the diagonal section method for calculation. In Fig. 19, it is the force analysis of soil strip unit $u_9u_{10}u_{11}u_{12}$. u_9u_{10} receives the force e_2 from the wall back, and the dip angle with the horizontal direction is $\pi/2-\alpha_2+\varphi$. u_9u_{12} and $u_{10}u_{11}$ are subjected to the forces S_2 and S_2+dS_2, respectively, and the dip angles to the horizontal direction are $\pi/2-\alpha_0+\varphi$. $u_{11}u_{12}$ is subjected to the force e_{21} in the CIJK region, and the dip angle to the horizontal direction is $\pi/2-\alpha_3+\varphi$.

Horizontal direction

$$e_2\frac{dz}{\sin\alpha_2}\cos\theta_2=k_h dw+dS_2\cos\theta_0+e_{21}\frac{dz\sin(\alpha_0+\alpha_2)}{\sin\alpha_2\sin(\alpha_0+\alpha_3)}\cos\theta_3 \tag{51}$$

Vertical direction

$$e_2\frac{dz}{\sin\alpha_2}\sin\theta_2+dS_2\sin\theta_0=(1-k_v)dw+e_{21}\frac{dz\sin(\alpha_0+\alpha_2)}{\sin\alpha_2\sin(\alpha_0+\alpha_3)}\sin\theta_3 \tag{52}$$

Where

$$\theta_0=\pi/2-\alpha_0+\varphi \tag{53}$$

$$dw=\frac{1}{2}\left(\frac{h_2}{\sin\alpha_0}+\frac{h_2+dz-l_u\sin\alpha 3}{\sin\alpha_0}\right)\gamma\frac{dz}{\sin\alpha_2}\sin(\alpha_0+\alpha_2) \tag{54}$$

$$h_2=\frac{z(\cot\alpha_3-\cot\alpha_2)-(m+0.06)H\cot\alpha_3+(l-n)H+0.9H\cot\alpha_2}{\cot\alpha_0+\cot\alpha_3} \tag{55}$$

l_u is the distance between edges $u_{11}u_{12}$

$$l_u=\frac{dz\sin(\alpha_0+\alpha_2)}{\sin\alpha_2\sin(\alpha_0+\alpha_3)} \tag{56}$$

Ignoring the second-order differential variables

$$dw=\gamma h_2 dz(\cot\alpha_0+\cot\alpha_2) \tag{57}$$

Combined with Eqs. (51)-(52) and Eq. (57), it is obtained

$$e_2=C_3\gamma h_2+C_4 e_{21}\big|_{z-h_2}\quad (m+0.06)H+h_r\le z<0.9H \tag{58}$$

It should be noted that when the depth of e_2 from the fill surface is z, the distance of e_{21} from the fill surface is z-h_2. Among them

$$\begin{cases}C_3=\sin\alpha_2(\cot\alpha_0+\cot\alpha_2)\dfrac{k_h\sin\theta_0+(1-k_v)\cos\theta_0}{\sin(\theta_0+\theta_2)}\\ C_4=\dfrac{\sin(\theta_0+\theta_3)\sin(\alpha_0+\alpha_2)}{\sin(\theta_0+\theta_2)\sin(\alpha_0+\alpha_3)}\end{cases} \tag{59}$$

The E_s of region FGMC is as follows

$$E_2=\int_{(m+0.06)H+h_r}^{0.9H}e_2dz \tag{60}$$

The resultant force's position is as follows

$$Z_2=\frac{\int_{(m+0.06)H+h_r}^{0.9H}e_2(H-z)dz}{E_2} \tag{61}$$

3.3.3 Calculation in the GHIM area

The left side of the GHIM area is completely vertical and in contact with the wall heel, while the right side extends from the bottom of the heel with a dip angle of α_0. As shown in Fig. 20, any soil strip in the region is taken for analysis. $u_{13}u_{14}$ receives the force e_{w2} from the wall heel, and the angle from the horizontal direction is δ. $u_{13}u_{16}$ and $u_{14}u_{15}$ are subjected to S_{w2} and $S_{w2}+dS_{w2}$ forces between soil strips, respectively, and the angle to the horizontal direction is $\pi/2-\alpha_0+\varphi$. e_{21} also affects the $u_{15}u_{16}$ side, and the distance between e_{w2} and e_{21} in the vertical direction is h_{w2}. The soil strip itself is subjected to two directions of force $k_h dw$ and $(1-k_v)dw$.

Horizontal direction

$$e_{w2}dz\cos\delta=k_h dw+dS_{w2}\cos\theta_0+e_{21}\cos\theta_3\frac{dz\cos\alpha 0}{\sin(\alpha_0+\alpha_3)} \tag{62}$$

Vertical direction

$$e_{w2}dz\sin\delta+dS_{w2}\sin\theta_0=(1-k_v)dw+e_{21}\sin\theta_3\frac{dz\cos\alpha 0}{\sin(\alpha_0+\alpha_3)} \tag{63}$$

$$dw=\frac{1}{2}\gamma dz\cot\alpha_0\left[2h_{w2}+dz\left(1-\frac{\sin\alpha_0\sin\alpha_3}{\sin(\alpha_0+\alpha_3)}\right)\right] \tag{64}$$

Ignoring the second-order differential variables

$$dw=\gamma h_{w2}dz\cot\alpha_0 \tag{65}$$

$$h_{w2}=\frac{z\cot\alpha_3-(m+0.06)H\cot\alpha_3+(l-n)H}{\cot\alpha_0+\cot\alpha_3} \tag{66}$$

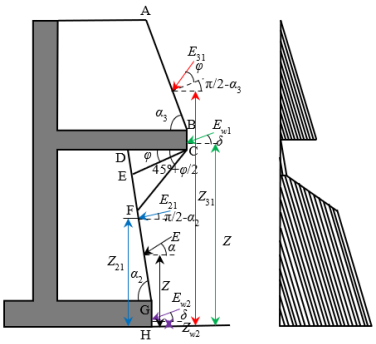

Fig. 21 Application points of earth pressure and resultant force in each region of long relief shelf

$$e_{w2} = C_{w21}\gamma h_{w2} + C_{w22}\, e_{21}\big|_{z-h_2} \tag{67}$$

$$C_{w21} = \frac{\cot\alpha_0\left[(1-k_v)\cos\theta_0 + k_h\sin\theta_0\right]}{\sin(\delta+\theta_0)} \tag{68}$$

$$C_{w22} = \frac{\cos\alpha_0\sin(\theta_0+\theta_3)}{\sin(\delta+\theta_0)\sin(\alpha_0+\alpha_3)} \tag{69}$$

The E_s of the GHIM area is expressed as follows

$$E_{w2} = \int_{0.9H}^{H} e_{w2}\,dz \tag{70}$$

The resultant force's position is as follows

$$Z_{w2} = \frac{\int_{0.9H}^{H} e_{w2}(H-z)\,dz}{E_{w2}} \tag{71}$$

3.3.4 The total resultant force of Es and its point of application under the the unloading effect

In Fig. 21, the operating points of each earth pressure under unloading effects are shown. It's worth noting that the effects do not affect the resultant forces E_{31} and E_{w1} in the upper section. E_{21} acts on the lower imaginary wall back, which can be solved in three parts, namely, the unloading effect region (DE), the excessive region (EF), and the region not affected by the unloading effect (FG). The normal earth pressure acting on DE and FG may be calculated using Eqs. (50) and (58). The normal earth pressure σ_{nt} acting on EF may be calculated using linear difference. Lastly, integral may be utilized to calculate DG's earth pressure E_{21}. The resultant force exerted by the earth pressure on the retaining wall, as well as the position of its application point, are eventually determined.

When at point E, Eq. (50) can be used to obtain normal earth pressure. When at point F, Eq. (58) can be used to obtain the normal earth pressure. The value of E_{21} can be calculated using the following formula.

$$\begin{cases} \sigma_{nt} = \dfrac{e_2\cos\varphi\big|_{(m+0.06)H+h_r} - \sigma_{nr}\big|_{(m+0.06)H+h_0}}{h_r - h_0}\left[z - \left((m+0.06)H + h_0\right)\right] \\ \quad + \sigma_{nr}\big|_{(m+0.06)H+h_0} \quad (m+0.06)H + h_0 \le z < (m+0.06)H + h_r \\ h_0 = h_r\dfrac{\cot(45°+\varphi/2)+\cot\alpha_2}{\cot\varphi+\cot\alpha_2} \end{cases} \tag{72}$$

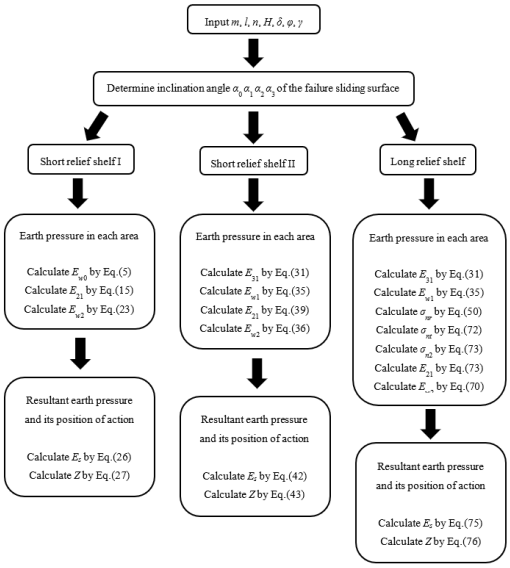

Fig. 22 Calculation process

$$\begin{cases} E_{21} = \int_{(m+0.06)H}^{(m+0.06)H+h_0}\sigma_{nr}dz + \int_{(m+0.06)H+h_0}^{(m+0.06)H+h_r}\sigma_{nt}dz + \int_{(m+0.06)H+h_r}^{0.9H}\sigma_{n2}dz \\ \sigma_{n2} = e_2\cos\varphi \end{cases} \tag{73}$$

By decomposing the earth pressure in each region and achieving equilibrium of the bending moment around the wall heel, the pseudo-static resultant force E and its application point for the entire retaining wall can be determined

$$\begin{cases} E_{31}\cos\theta_3 + E_{w1}\cos\delta + E_{21}\sin\alpha_2 + E_{w2}\cos\delta = E\cos\alpha \\ E_{31}\sin\theta_3 + E_{w1}\sin\delta + E_{21}\cos\alpha_2 + E_{w2}\sin\delta = E\sin\alpha \end{cases} \tag{74}$$

$$\begin{cases} E_s = \dfrac{E_{31}\cos\theta_3 + E_{w1}\cos\delta + E_{21}\sin\alpha_2 + E_{w2}\cos\delta}{\cos\alpha} \\ \alpha = \arctan\dfrac{E_{31}\sin\theta_3 + E_{w1}\sin\delta + E_{21}\cos\alpha_2 + E_{w2}\sin\delta}{E_{31}\cos\theta_3 + E_{w1}\cos\delta + E_{21}\sin\alpha_2 + E_{w2}\cos\delta} \end{cases} \tag{75}$$

$$\begin{cases} Z = \dfrac{0.1H\cot\alpha_2}{\cot\alpha+\cot\alpha_2} + \dfrac{M_{31}+M_{w1}+M_{21}+M_{w2}}{E(\cos\alpha+\cot\alpha_2\sin\alpha)} \\ M_{31} = E_{31}Z_{31}\cos\theta_3 + E_{31}\left[0.5(H-Z_{31})\cot\alpha_3 + (n-l)H\right] \\ M_{w1} = E_{w1}\left[Z_{w1}\cos\delta + (n-l)H\sin\delta\right] \\ M_{21} = E_{21}\left[Z_{21}\sin\alpha_2 + (Z_{21}-0.1H)\cot\alpha_2\cos\alpha_2\right] \\ M_{w2} = E_{w2}Z_{w2}\cos\delta \end{cases} \tag{76}$$

4. Calculation process

Fig. 22 shows the calculation process for determining the earth pressure acting on the retaining wall. By inputting the initial parameters, the angle of each sliding surface in the plastic region is obtained, and the corresponding failure mode is determined. The resultant force and the position of the active point of the pseudo-static force are then obtained by the formula.

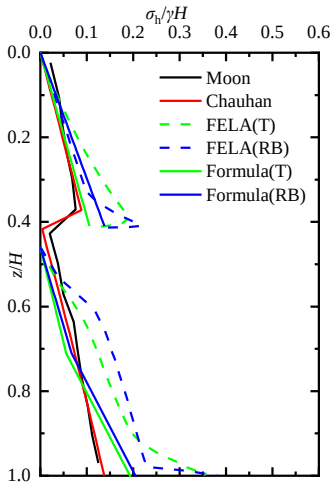

Fig. 23 Comparison and verification of earth pressure under various conditions

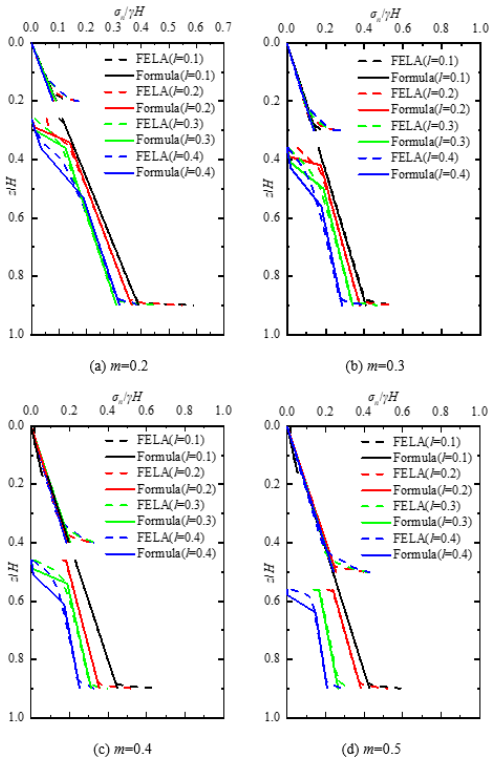

Fig. 24 Comparison and verification of earth pressure distribution under the change of relief shelf length and position

5. Contrast verification

5.1 Case 1

The current research about retaining walls primarily focuses on the translational displacement mode. The study on the pseudo-static force of unloading retaining wall rotating around the wall heel is still in the initial stage, and almost no data are available for investigation. Therefore, the experimental data of Moon *et al.* (2013) and the numerical simulation data of Chauhan and Dasaka (2021) are used in this paper as reference objects to verify the theoretical formula's accuracy without considering the seismic acceleration, and the reliability of the pseudo-static solution is obtained from the side. Firstly, FELA software OptumG2 was used for modeling according to the experimental data of Moon *et al.* The parameters of the model are as follows: retaining wall height =1.2 m, unloading plate position m = 0.4, and unloading plate length b =(H-h)tanψ, where ψ = (45°+φ/2). The filling behind the wall is sandy soil with an internal friction angle and a heavy load of 38.4° and 15.41 kN/m^3, respectively. Secondly, the lateral earth pressure distribution obtained by the FELA and theoretical formula is compared with the results obtained by Moon *et al.* (2013), and Chauhan and Dasaka (2021), as shown in Fig. 23. It should be noted that Moon *et al.* (2013) reported the lateral earth pressure distribution of the actual retaining wall. Moreover, the unloading effect area and transition area should be extended from the imaginary wall back to the actual wall back when solving the problem with the theoretical formula. This would lead to the expansion of the range of the unloading effect area and transition area and the change of the lateral earth pressure distribution. Specifically, the lower retaining wall is directly covered by the unloading effect area and the transition area or is completely or partially affected by the unloading effect, and the earth pressure presents a broken line distribution.

The FELA software and the theoretical formula are used to give the corresponding soil pressure distribution in Fig. 23 to study the difference of lateral earth pressure distribution under different displacement modes and the applicability of the theoretical formula under T and RB displacement modes. Above the unloading plate, the numerical and theoretical solutions of the earth pressure under the two displacement modes do not significantly differ from the results of Moon *et al.* (2013), Chauhan and Dasaka (2021). The stress deflects only when approaching the unloading plate gradually due to the action of the plate on the soil, and the earth pressure distribution presents a certain difference. Below the unloading plate, the theoretical solution of earth pressure under the two displacement modes is closer to the results of Moon *et al.* (2013), and Chauhan and Dasaka (2021); however, the corresponding numerical solution of earth pressure is larger.

The earth pressure distribution comparison under the T and RB displacement modes showed that the earth pressure distribution under the two conditions is similar. Under the unloading plate, the lateral earth pressure corresponding to RB mode is greater than that of the T mode in both numerical and theoretical solutions, indicating that the unloading effect has a more significant influence on the earth pressure in the T mode. In general, the displacement model only changes the magnitude of earth pressure but basically doesn't affect the *distribution*

5.2 Case 2

The comparison between the numerical solution and theoretical solution of the earth pressure distribution aimed to investigate the influence of geometric parameters of the

unloading plate on the accuracy of the derived formula. Since many factors affect the quasi-static force of the retaining wall (Ouria *et al.* 2016), the method of control variables is adopted. This section only studies the influence of the geometric conditions of the unloading plate. The model corresponding to the numerical solution is shown in the figure. (α= 30°, m=0.3, k_h=0.1, k_v=0.1), and the physical properties and other parameters of the foundation soil remain unchanged. The position of the unloading plate increases from 0.2 times the wall height to 0.5 times from the top of the wall, and the length gradually increases from 0.1 times the wall height to 0.4 times. Draw the pseudo-static distribution function obtained by two calculation methods at different positions and RS's lengths, as shown in Fig. 24.

As the figure, the earth pressure distribution can be divided into the upper and lower part of the RS due to its location setting. In the upper part, the earth pressure distribution only has a certain error in a small range close to the unloading plate, with a good overall performance. In the lower part, the earth pressure distribution deviates in the influence range of the unloading effect (i.e., the unloading area and the transition area) and near the wall heel. In other areas, the distribution of the two kinds is consistent. It can be found that when the wall rotates around the wall heel, the existence of the RS and the heel floor of the wall will cause a disturbance to the soil mass, causing stress deflection and resulting in the error of the earth pressure distribution. As the RS is set down along the vertical arm, the material of the plate needs to be considered to prevent deformation due to excessive soil load. As the length of the RS increases, the unloading effect's influence becomes more significant, and the earth pressure decreases gradually.

It should be noted that the RS's length is short and not far from the wall heel when m = 0.5 and l = 0.1 in the figure. The sliding surface in the plastic zone is directly in contact with the retaining wall arm over the RS, which is consistent with the sliding surface's distribution behind the cantilever retaining wall. It is proved that this formula can be used to solve the quasi-static force of the cantilever retaining wall under seismic acceleration.

6. Parametric analysis

By conducting numerical simulations and comparing with relevant previous cases, the aforementioned study provides evidence to support the reliability of using the inclined slice method to determine the pseudo-static solution of retaining walls under seismic effects. The pseudo-static solution under different conditions is obtained through the theoretical formula to study the stress of the unloaded retaining wall when the parameters change. The pseudo-static solution and the numerical solution are dimensionless treated, and the approach provides a distribution of normal earth pressure along the height of the wall. By utilizing theoretical formulas, it is possible to obtain the resultant force and the corresponding diagram indicating the position of the force point.

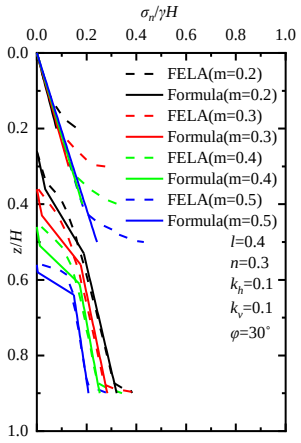

Fig. 25 Influence of relief shelf position change on earth pressure distribution

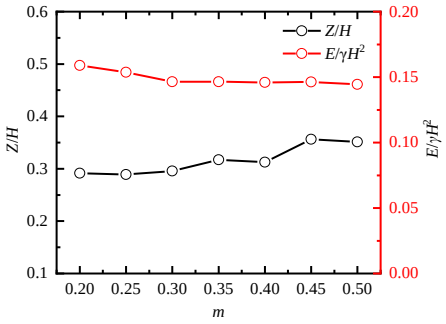

Fig. 26 Influence of relief shelf position change on resultant force and application point

6.1 Relief shelf position

Figs. 25 and 26 illustrate the earth pressure distribution and the variation of the point of application of the resultant force as the position of the RS increases from 0.2 to 0.5, respectively.

As shown in Fig. 25, increasing the depth of the upper portion of the retaining wall will result in an increase in the E_s exerted on the wall. On the contrary, the height of the lower wall of the RS, the influence range of the unloading effect area and the transition area, and the E_s are reduced.

Combined with the upper and lower parts of the unloading plate, it is speculated that the total E_s is gradually decreasing, which is verified in Fig. 26. As the relative position of the RS increases from 0.2 to 0.5, the resultant force decreases by 9.2%. Additionally, the position of the resultant force shifts towards the upper third of the wall height.

6.2 Relief shelf length

Figs. 27 and 28 depict the distribution of earth pressure and the variation of the point of application of the resultant force as the length of RS changes, respectively.

As depicted in Fig. 27, the length does not significantly affect the distribution of earth pressure in the upper part of the RS. It should be noted that when l = 0.1, an abrupt shift

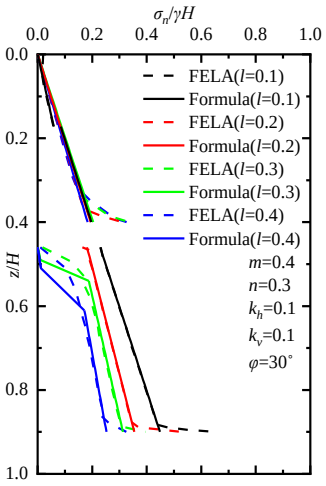

Fig. 27 Influence of relief shelf length change on earth pressure distribution

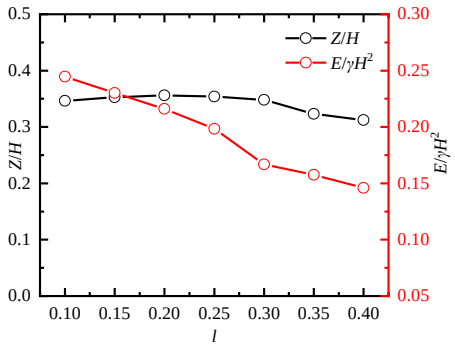

Fig. 28 Influence of relief shelf length change on resultant force and application point

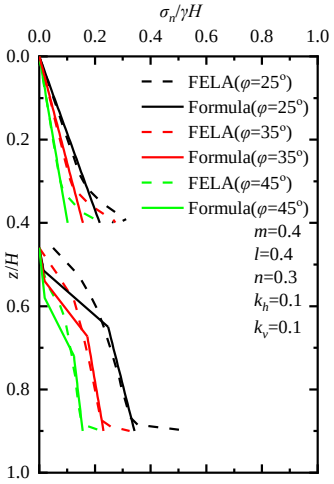

Fig. 29 Influence of internal friction angle change on earth pressure distribution

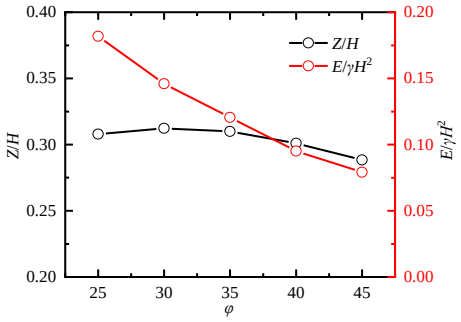

Fig. 30 Influence of internal friction angle change on earth pressure distribution

in the distribution of ground pressure occurs when the sliding surface makes contact with the retaining wall arm. In the lower region of the unloading plate, with the increase of the length of the unloading plate, the unloading effect begins to play a role and gradually becomes significant, which is manifested in the decrease of the normal earth pressure in the lower region.

In Fig. 28, The resulting force of the retaining wall's seismic active ground pressure diminishes with plate length. which also proves this phenomenon. Increasing the relative length of RS from 0.1 to 0.4 leads to a 40.4% decrease in the resultant force of the earth pressure. Initially, the resultant force's position remains unchanged, but then it slightly decreases.

6.3 Backfilled soil internal friction angle

The soil's internal friction angle is an indicator of the roughness of soil particle surfaces. A higher internal friction angle implies a greater resistance to sliding between soil particles, resulting in increased shear strength. Fig. 29 illustrates the normal earth pressure distribution on a retaining wall varying with changes in the internal friction angle. Fig. 30 depicts the effect of altering the internal friction angle of the backfill soil on the resultant force and location of the action point of E_s.

As shown in Fig. 29, the increase of internal friction angle will reduce the normal earth pressure on the upper and lower parts of the unloading plate. The change of internal friction angle will not affect the distribution but will increase the range of unloading effect area.

In Fig. 32, as the internal friction angle increases, the resultant force of earth pressure tends to decrease. As the angle of internal friction rises from 25° to 45°, the resultant force decreases by 56.5%. Moreover, the position of its action point gradually decreases with the increase of internal friction angle.

6.4 Horizontal seismic acceleration coefficient

Seismic load can lead to significant damage to retaining walls and other structures. To investigate the retaining walls's earth pressure under active limit state conditions, seismic acceleration simulation is employed. Figs. 31 and 34. show the normal earth pressure's distribution under horizontal seismic acceleration and the magnitude and position of the resultant force under horizontal seismic acceleration, respectively.

According to Fig. 31, the normal earth pressure of the retaining wall in the top half of the unloading plate is unaffected by the increase in seismic horizontal acceleration, and the normal pressure in the lower region beneath the unloading plate exhibits an increasing trend.

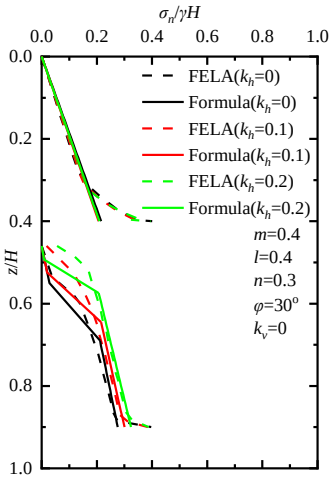

Fig. 31 Influence of horizontal seismic acceleration on earth pressure distribution

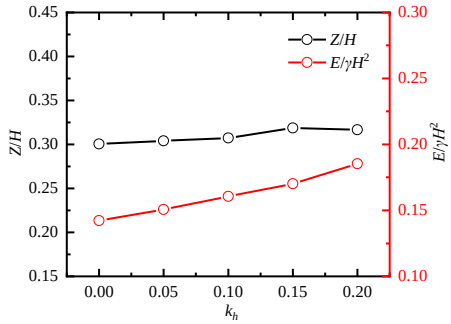

Fig. 32 Effect of horizontal seismic acceleration on resultant force and application point

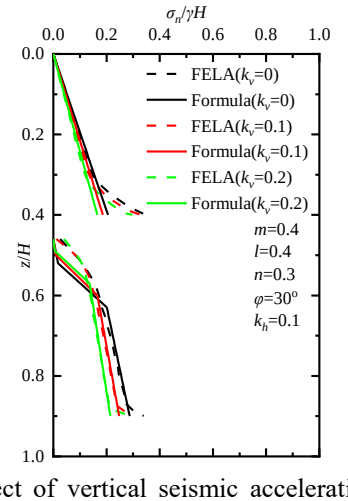

Fig. 33 Effect of vertical seismic acceleration on earth pressure distribution

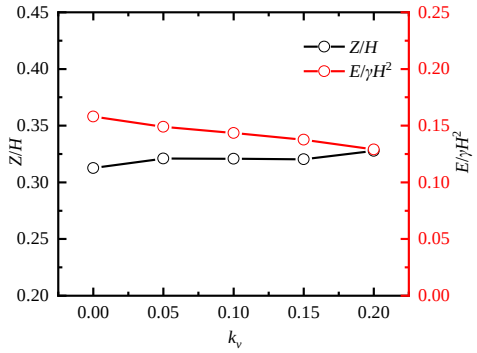

Fig. 34 Effect of vertical seismic acceleration on resultant force and application point

Moreover, during this process, the unloading area and transition zone continuously narrow down. Consequently, it is inferred that this diminishes the unloading action of the R S.

As can be seen in Fig. 32, as the seismic horizontal acceleration rises, so does the soil pressure that results, as well as a little shift in the direction of the resultant force. The resulting force increases by 30.4% as the acceleration rises from 0 to 0.2.

6.5 Vertical seismic acceleration coefficient

The vertical seismic acceleration is utilized to simulate the vertical seismic load on the retaining wall, and its influence on the E_s is analyzed. Fig. 33 indicates the normal earth pressure distribution when the vertical seismic acceleration increases. Fig. 34 shows the vertical seismic acceleration's effect on the resultant force and its action point position.

According to Fig. 35, the normal earth pressure steadily drops as the vertical seismic acceleration increases in both the higher and lower portions of the unloading plate. Moreover, the range of the unloading impact region and transition area likewise shrinks. It may be deduced that when vertical seismic acceleration increases, the resultant force drops and has a weakening influence on the unloading action of the unloading plate.

The above assertion is supported by the variation trend of the resultant force with vertical seismic acceleration displayed in Fig. 36. When the vertical seismic acceleration rises, so does the position of the resulting force action point. When the acceleration *coefficient* increases from 0 to 0.2, the resultant force decreases by 18.4%.

In summary, k_h and k_v have opposite effects on the resultant force of E_s, with the k_h exerting a more pronounced impact.

7. Conclusions

•The investigation utilizing finite element shear dissipation demonstrates that, when subjected to seismic loading, the backfill soil behind the unloading retaining wall undergoes active failure, resulting in the formation of regular sliding wedges and corresponding sliding surfaces. Through comprehensive analysis, three fundamental failure modes are identified and extensively examined in this study. The inclined strip method, in conjunction with the wedge limit equilibrium theory, is employed to derive a quasi-static solution for the active state of the retaining wall, which serves as a valuable comparative reference.

• The results of parameter analysis show that the increase in

the RS's length and position, the internal friction angle of the filling soil, and the vertical seismic acceleration reduce the E_s. The influence of the horizontal seismic acceleration on the E_s is opposite. It should be noted that the increase of some parameters will gradually reduce the range of unloading area and transition area under the unloading plate and will weaken the unloading effect to a certain extent. The length of RS and the internal friction angle of the fill will both boost the unloading impact.

• Compared with the other factors, the influence of the RS's length, the soil's internal friction angle, and the horizontal seismic acceleration all have a more significant influence on the resulting earth pressure. When l increases to 0.4, φ increases to 45°, and k_h increases to 0.2, the resultant earth pressure decreases by 40.4%, decreases by 56.5%, and increases by 30.4%. Each factor has a little effect on the position of the resultant force, which is largely maintained near the height of one-third of the wall.

• The derived formula in this study is applicable to both static and seismic loading conditions, displaying a high level of accuracy and providing valuable references for engineering design. However, owing to the necessary simplifications in the model, the influence of soil anisotropy and pseudo-dynamic calculation results on the earth pressure behind the wall is not considered in this paper, which is also the focus of future research.

Acknowledgments

The authors acknowledge the financial support provided by National Natural Science Foundation of China (Grant No. 41772297).

References

Bahmani Tajani, S., Fathipour, H., Payan, M., Jamshidi Chenari, R. and Senetakis, K. (2022), "Temperature-dependent lateral earth pressures in partially saturated backfills", *Eur. J. Environ. Civil Eng.*, **27**(10), 3064-3090. https://doi.org/10.1080/19648189.2022.2125911.

Cao, W.G., Liu, T. and Xu, Z. (2019), "Calculation of passive earth pressure using the simplified principal stress trajectory method on rigid retaining walls", *Comput. Geotech.*, (109), 108-116. https://doi.org/10.1016/j.compgeo.2019.01.021.

Chauhan, V.B. and Dasaka, S.M. (2021), "Active earth pressure on retaining wall with a relief shelf: a novel analytical method", *Innov. Infrastruct. Solutions*, **7**(1). https://doi.org/10.1007/S41062-021-00690-Y.

Chauhan, V.B. and Dasaka, S.M. (2016), "Behaviour of rigid retaining wall with relief shelves with cohesive backfill", *Proceedings of the 5th Int Conf Forensic Geot Eng, Bangalore*, India.

Choudhury, D. and Singh, S. (2006), "New approach for estimation of static and seismic active earth pressure", *Geotech. Geol. Eng.*, **24**, 117-127. https://doi.org/10.1007/s10706-004-2366-x.

Coulomb, C.A. (1776), "Essai sur une application des règles de maximis et minimis à quelques problèmes de stratique relatifs à 1'architecture", *Mémoires de Mathematique et de Physique Presentes a l'Académie Royale des Sciences*, Paris(7), 343-382.

Fathipour, H., Tajani, S.B., Payan, M., Chenari, R.J. and Senetakis, K. (2022), "Influence of transient flow during infiltration and isotropic/anisotropic matric suction on the passive/active lateral earth pressures of partially saturated soils". *Eng. Geol.*, 310. https://doi.org/10.1016/j.enggeo.2022.106883.

Fathipour, H., Payan, M., Chenar, R.J. and Senetakis, K. (2021), "Lower bound analysis of modified pseudo-dynamic lateral earth pressures for retaining wall-backfill system with depth-varying damping using fem-second order cone programming", *Int. J. Numer. Anal. Method. Geomech.*, https://doi.org/10.1002/nag.3269.

Fathipour, H., Payan, M., Siahmazgi, A.S. and Veiskarami, M (2021), "Limit analysis of modified pseudodynamic lateral earth pressure in anisotropic frictional medium using finite-element and second-order cone programming", *Int. J. Geomech.*, https://doi.org/21(2).10.1061/(ASCE)GM.1943-5622.0001924.

Greco, V.R. (2009), "Seismic active thrust on cantilever walls with short heel", *Soil Dynam. Earthq. Eng.*, **29**(2), 249-252.

Iskander, M., Chen, Z., Omidvar, M., Guzman, I. and Elsherif, O (2013), "Active static and seismic earth pressure for c-psi soils", *Soils Found.*, **53**(5), 639-652. https://doi.org/10.1016/j.sandf.2013.08.003.

Johari, A., Javadi, A.A. and Najafi, H. (2016), "A genetic-based model to predict maximum lateral displacement of retaining wall in granular soil", *Scientia Iranica*, **23**(1), 54-65. https://doi.org/10.24200/sci.2016.2097.

Johari, A. and Maroufi, M. (2024), "System reliability analysis of geogrid reinforced retaining wall using random finite element method", *Transport. Geotech.*, **48**, 101316-101316. https://doi.org/10.1016/j.trgeo.2024.101316. .

Kerisel, J. and Absi, E. (1990), "Active and passive earth pressure tables", *A.A. Balkema, Rotterdam*

Klein, G.K. (1964), "Calculation of retaining wells", *Moscow:Vysshaya Shkola.(in Russian)*.

Lim, H., Park, J., Kim, J. and Ko, J. (2023), "Numerical study on stability and deformation of retaining wall according to groundwater drawdown", *Geomech. Eng.*, **33**(2), 195-202. https://doi.org/10.12989/gae.2023.33.2.195.

Moon, I.J., Kim, B.I., Yoo, W.K. and Park, Y.S. (2013), "Model tests for measurement of lateral earth pressure on retaining wall with the relieving platform using jumoonjin sand", *J. Korea Academia-Ind. Cooperation Soc.*, **14**(11), 55-55. https://doi.org/10.5762/kais.2013.14.11.5923.

Mohamad, S.M., Hamid, S.L., Mohammad, S.M., Payan, M. and Chenari, R.J. (2021), "Active lateral earth pressure of geosynthetic-reinforced retaining walls with inherently anisotropic frictional backfills subjected to strip footingloading", *Comput. Geotech.*, 137. https://doi.org/10.1016/J.COMPGEO.2021.104302.

Nakajima, S., Ozaki, T. and Sanagawa, T. (2021), "1 g Shaking table model tests on seismic active earth pressure acting on retaining wall with cohesive backfill soil", *Soils Found.*, **61**(5), 1251-1272. https://doi.org/10.1016/J.SANDF.2021.06.014.

Ouria, A., Toufigh, V., Desai, C., Toufigh, V. and Saadatmanesh, H. (2016), "Finite element analysis of a CFRP reinforced retaining wall", *Geomech. Eng.*, **10**(6), 757-774. https://doi.org/10.12989/gae.2016.10.6.757.

Pain, A., Choudhury, D. and Bhattacharyya, K.S. (2015), "Seismic stability of retaining wall–soil sliding interaction using modified pseudo-dynamic method", *Géotech. Lett.*, 5(1), 56-61. https://doi.org/10.1680/geolett.14.00116.

Peng, J. (2022), "Modified Horizontal Slice Element Method for Active Earth Pressure Against Rigid Retaining Walls". *Soil Mech. Found. Eng.*, **59**(5), 484-491. https://doi.org/10.1007/S11204-022-09840-5.

Peng, M.X. and Chen, J. (2013), "Coulomb's solution to seismic passive earth pressure on retaining walls", *Can. Geotech. J.*,

50(10), 1100-1107. https://doi.org/10.1139/cgj-2012-0392.

Que, Y., Gui, X.F. and Chen, F.Q. (2022), "Active earth pressure against cantilever retaining walls with the long relief shelf rotating about the nottom", *Int. J. Geomech*., **22**(10). https://doi.org/10.1061/(ASCE)GM.1943-5622.0002524.

Srikar, G. and Mittal, S. (2021), "Modified pseudo-dynamic analysis of rigid gravity retaining wall with cohesion-less backfill and uniform surcharge", *Geomech. Eng.*, **26**(5), 453-464. https://doi.org/10.12989/gae.2021.26.5.453.

Terzaghi, K. (1943), "Theoretical soil mechanics", John Wiley and Sons, New York.

Thiyyakkandi, S., Shankar, P., Neeraj, C.R. and Lukose, A. (2021), "Active earth pressure on retaining walls with sloping backfill considering arching effect under rotation about base", *Innov. Infrastruct Solution*, **7**(1). https://doi.org/10.1007/S41062-021-00724-5.

Wang, Z.Y., Liu, X.X., Wang, W.W., Tao, Z.Y. and Li, S. (2022), "Inclined layer method-based theoretical calculation of active earth pressure of a finite-width soil for a rotating-base Retaining wall", *Sustainability*, **14**(15), 9772-9772. https://doi.org/10.3390/SU14159772.

Xu, L., Zhang, Y.B., Chen, F.Q. and Lin, Y.J. (2021), "Active Earth Pressure of Narrow Backfill on Inverted T-Type Retaining Walls under Translation Mode", *Int. J. Geomech*., **21**(11). https://doi.org/10.1061/(ASCE)GM.1943-5622.0002176.

Yang, K.H. and Liu, C.N. (2007), "Finite element analysis of earth pressures for narrow retaining walls", *J. Geoeng.*, **2**(2), 43-52. https://doi.org/10.6310/jog.2007.2(2).1.

Zhang, Y.B., Chen, F.Q., Lin, Y.J. and Chen, H.B. (2022), "Active earth pressure of narrow backfill against inverted T-type retaining walls rotating about the heel", *KSCE J. Civil Eng.*, 1-17. https://doi.org/10.1007/S12205-022-1294-8.

CC

Notations

b = Length of relief shelf (m)

b_1 = Length of wall toe (m)

b_2 = Thickness of wall stem (m)

b_3 = Length of wall heel (m)

l = Relative length of relief shelf

m = Relative height of upper wall

n = Relative length of wall heel

c = Cohesion of soil (kPa)

E = Young's modulus (MPa)

H = Total height of wall (m)

H_1 = Height of upper wall (m)

H_2 = Thickness of relief shelf (m)

H_3 = Height of lower wall (m)

H_4 = Thickness of bottom plate (m)

α = The slip plane and the horizontal plane angle (°)

α_0 = The angle between FGMC region and horizontal plane (°)

α_1 = First failure surface inclination (°)

α_2 = Second failure surface inclination (°)

α_3 = Third failure surface inclination (°)

δ = Friction of the soil–wall interface (°)

φ = Internal friction of soil (°)

γ = Unit weight of soil (kN/m^3)

σ_n = Lateral earth pressure (kPa)

μ = The total displacement at the top of the wall (m)

E_{w0} = Reaction force of sliding wedge on retaining wall (kN)

E_{w1} = Reaction force of sliding wedge on retaining wall (kN)

E_{w2} = The resultant earth pressure at the heel in short RS (kN)

E_{21} = The resultant force acting on the imaginary wall back in short RS (kN)

E_{31} = The resultant force of the imaginary wall back on the block above RS (kN)

E_a = Active earth pressure (kN)

E_s = The seismic active earth pressure (kN)

E = Total earth pressure acting on retaining wall (kN)

E_r = The force of the imaginary wall back on the block in long RS (kN)

e_{21} = The force of the hypothetical wall back to the soil strip (kN)

e_{w2} = The force of wall heel to sliding wedge (kN)

e_2 = The force of the imaginary wall back under RS on the block (kN)

h_{w2} = The distance between e_{w2} and e_{21} in the vertical direction (m)

K = Coefficient of normal earth pressure

K_{31} = The normal earth pressure coefficient for the imaginary wall back in short RS

K_r = The normal earth pressure coefficient of the imaginary wall back in long RS

k_h = Horizontal seismic acceleration coefficient

k_v = Vertical seismic acceleration coefficient

M_{w0} = Bending moment in the ABG area (kN·m)

M_{w1} = Bending moment in the BCLK area (kN·m)

M_{w2} = Bending moment in the CDEF area (kN·m)

M_{21} = Bending moment in the BCFG area (kN·m)

M_{31} = Bending moment in the ABI area (kN·m)

S_1 = The force between soils in the BCFG area (kN)

S_2 = The force between soils in the FGMC area (kN)

S_3 = The force between soils in the ABI area (kN)

S_r = The force between soils in the DFC region (kN)

S_{w1} = The force between soils in the ABG area (kN)

S_{w2} = The force between soils in the CDEF area (kN)

v = Poisson's ratio of soil

dw = Weight of soil element

W_0 = The self-weight of block in the ABG area (kN)

W_r = The self-weight of block in the DFC area (kN)

Z_{w0} = The action point location of the resultant force in the ABG area (m)

Z_{w1} = The action point location of the resultant force in the BCHI area (m)

Z_{w2} = The action point location of the resultant force in the DEFG area (m)

Z_{21} = The action point location of the resultant force in the BCFG area (m)

Z_{31} = The action point location of the resultant force in the CDGH area (m)